J. Biophotonics **7**, No. 6, 401–409 (2014) / **DOI** 10.1002/jbio.201200155

Journal of BIOPHOTONICS

FULL ARTICLE

Molecular photoacoustic tomography of breast cancer using receptor targeted magnetic iron oxide nanoparticles as contrast agents

Lei Xi[1], *Stephen R. Grobmyer*[2], *Guangyin Zhou*[2], *Weiping Qian*[3], *Lily Yang*[3], *and Huabei Jiang*[*,1]

[1] Department of Biomedical Engineering, University of Florida, College of Engineering JG56 BMS Bldg., Gainesville, FL 32611-6131, USA
[2] Department of Surgery, University of Florida, Gainesville, FL, 32611, USA
[3] Department of Surgery, Emory University, Atlanta, Georgia, 30322, USA

Received 14 August 2012, revised 2 October 2012, accepted 3 October 2012
Published online 1 November 2012

Key words: breast cancer, photoacoustic tomography, receptor-targeted magnetic iron oxide, nanoparticles, molecular imaging, fluorescence imaging

In this report, we present a breast imaging technique combining high-resolution near-infrared (NIR) light induced photoacoustic tomography (PAT) with NIR dye-labeled amino-terminal fragments of urokinase plasminogen activator receptor (uPAR) targeted magnetic iron oxide nanoparticles (NIR830-ATF-IONP) for breast cancer imaging using an orthotopic mouse mammary tumor model. We show that accumulation of the targeted nanoparticles in the tumor led to photoacoustic contrast enhancement due to the high absorption of iron oxide nanoparticles (IONP). NIR fluorescence images were used to validate specific delivery of NIR830-ATF-IONP to mouse mammary tumors. We found that systemic delivery of the targeted IONP produced 4- and 10-fold enhancement in photoacoustic signals in the tumor, compared to the tumor of the mice that received non-targeted IONP or control mice. The use of targeted nanoparticles allowed imaging of tumors located as deep as 3.1 cm beneath the normal tissues. Our study indicates the potential of the combination of photoacoustic tomography and receptor-targeted NIR830-ATF-IONP as a clinical tool that can provide improved specificity and sensitivity for breast cancer detection.

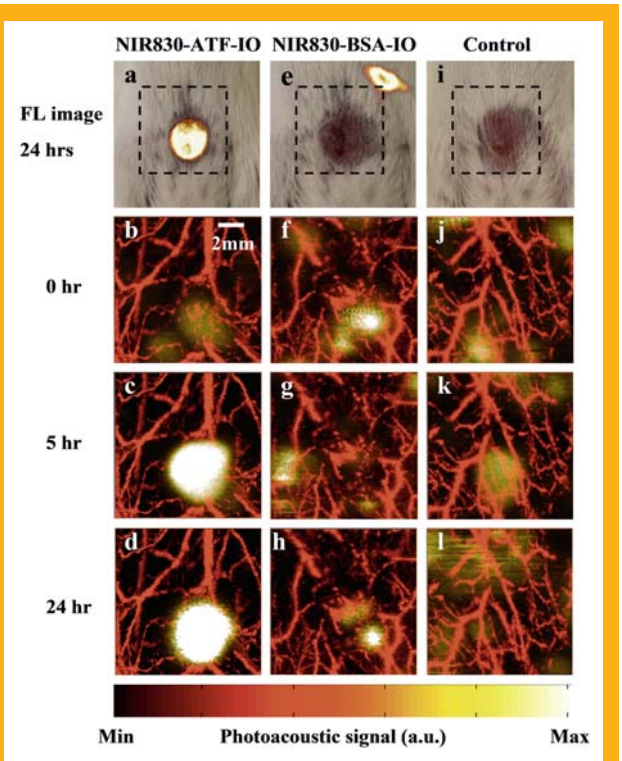

In vivo photoacoustic MAP and fluorescence images before and after injection. Micrographs were merged with fluorescence images taken 24 hours post injection with indicated agent (**a, e, i**). Panels **b** thru **l**. Photoacoustic MAP images were merged with images of blood vessels before injection (**b, f, j**), and at 5 hours (**c, g, k**) and 24 hours (**d, h, l**) post injection.

* Corresponding author: e-mail: hjiang@bme.ufl.edu, Phone: 352 273 9336, Fax: 352 273 9221

1. Introduction

Breast cancer affects 1 in 8 women in the U.S. and about 230480 new invasive breast cancer cases and 39520 breast cancer deaths were reported in 2011 [1–3]. Conventional breast imaging techniques such as X-ray, ultrasound and magnetic resonance imaging (MRI) have limitations. X-ray mammography is the most widely used and remains the imaging standard for breast cancer diagnosis, but exposes patients to ionization radiation, is not ideal for imaging dense breasts, which are typically associated with younger female patients (< 50 yr) [4]. Although ultrasound is very useful in characterizing breast lesions in dense breasts, it is not used as a primary screening method due to its low contrast level and specificity [5]. Breast MRI shows high sensitivity but low specificity producing a high false-positive rate [6]. Therefore, there is an urgent need to develop noninvasive, and highly sensitive and specific approaches with a high resolution for early detection, accurate diagnosis and precise resection of breast cancer.

Molecular imaging techniques using target-specific probes for positron emission tomography (PET) or single photon emission computed tomography (SPECT) have been demonstrated for breast cancer diagnosis and treatment monitoring [7–9]. These imaging methods have shown improved specificity and sensitivity in cancer detection, compared with conventional mammography. However, PET and SPECT have low spatial resolution in determining anatomic location of the tumor. Additionally, their dynamic and time-resolved imaging ability is limited because of the long half-life of the radiotracers. PET and SPECT both involve ionization radiation.

Photoacoustic tomography (PAT) is an imaging technique that detects wide-band acoustic waves that are generated when biological tissue absorbs short laser pulses. This imaging method has the advantages of high optical contrast as well as increased ratio of imaging depth to spatial resolution. The image resolution and maximum imaging depth can be adjusted with the ultrasonic frequency and the penetration of diffuse photons. The optical-to-acoustic conversion efficiency represents how many incident photons will be absorbed and converted to heat and how fast this heat can diffuse from the target during thermoelastic expansion and wave generation. As such, this conversion efficiency will determine the contrast intensity of photoacoustic imaging. Although an increase in hemoglobin (Hb) content in breast tumors results in enhanced absorption of photon energy that leads to 2 to 4 times higher photoacoustic signals, compared to the healthy breast tissue, the signal is not strong enough to detect breast tumors located deep below the skin [10–17]. To enhance the photoacoustic signals, contrast agents are used to generate acoustic transients. Several recent studies have reported the use of targeted and non-targeted contrast agents in imaging lymph nodes [18], melanomas [19], angiogenesis [20], the cerebral cortex [21] and brain tumors [22]. Iron oxide nanoparticles (IONP) have been widely used to enhance the image contrast for MRI in mice experiments and have recently been approved for pilot studies on humans. Amino-terminal fragments of uPA conjugated to iron oxide nanoparticles (ATF-IONP) have been used successfully in *in vivo* magnetic resonance imaging of mouse mammary tumors [23]. In this study, tumor cells selectively bound and internalized the ATF-IONP and provided high contrast for MRI. Galanzha et al. also demonstrated the use of IONP as a contrast agent to detect circulating tumor cells [24]. In our study, we used near-infrared dye labeled amino-terminal fragments of uPA conjugated to iron oxide nanoparticles (NIR830-ATF-IONP) to specifically bind to uPAR, a cellular receptor highly expressed in many types of human cancer tissues, including breast cancer.

2. Material and methods

2.1 Cell line

Mouse mammary carcinoma cell line 4T1 was used. Cells were cultured at 37 °C and 5% CO_2 in a humidified incubator in Dulbecco's Modified Eagle's Medium supplemented with 10% fetal bovine serum and antibiotics. Cells were harvested at 80% confluence.

2.2 Preparation of NIR830-ATF-IONP and control NIR830-bovine serum albumin-IONP (NIR830-BSA-IONP)

Recombinant amino-terminal fragments (ATF) were generated using from pET101/D-TOPO expression vectors containing a mouse ATF of the receptor binding domain of uPA cDNA sequence and expressed in E. coli BL21 (Invitrogen, Carlsbad, CA). ATF peptides were purified from bacterial extracts with Ni^{2+} nitrilotri-acetic acid (NTA)-agarose columns (Qiagen, Valencia, CA) using our established protocols [23]. IR-783 (Sigma-Aldrich, St. Louis, MO) was used to synthesize near-infrared dye (NIR-830) as described by Lipowska [25]. The schematic and spectral characterization (excitation wavelength: 800 nm and emission wavelength: 825 nm) of NIR-830 dye were shown in Figure 1a and c. Free thiol

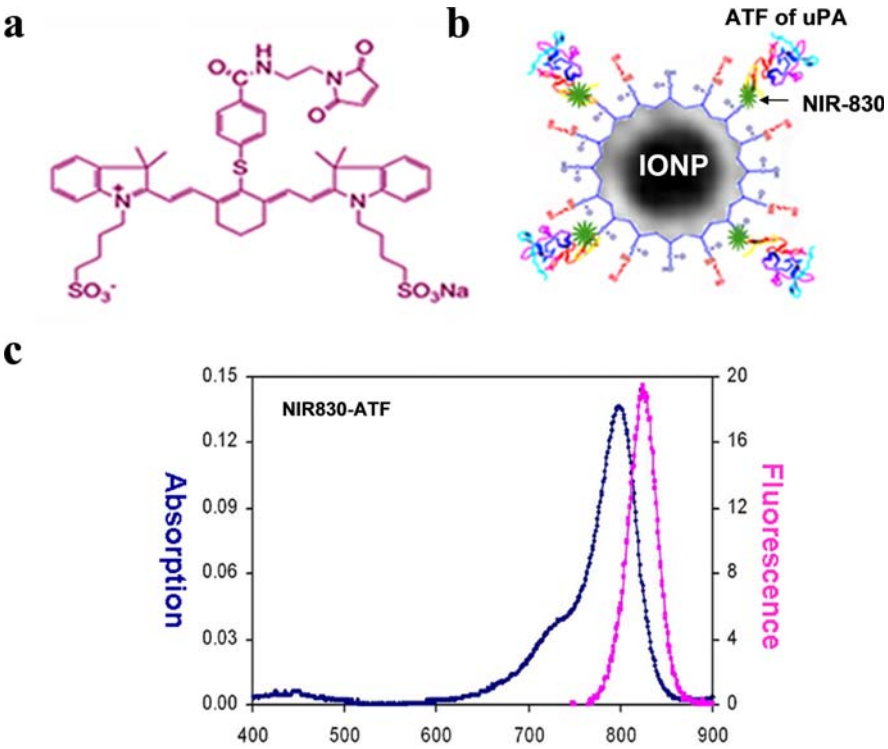

Figure 1 Illustration of NIR-830 dye and ATF-conjugated IONP probe. (**a**) Schematic of NIR-830 dye. (**b**) NIR 830 dye is conjugated to mouse ATF peptide through a bond between maleimide esters and free thiol groups of cystidine residues of the the peptide. Dye-labeled peptides were then conjugated to carboxyl group of the polymer coating on the IONPs. (**c**) Resulting optical probe has an Ex 800 nm and Em 825 nm.

groups on the ATF peptide or control bovin serum albumin protein (BSA) were labeled with NIR-830 dye and then conjugated to amphiphilic polymer-coated, 10 nm magnetic iron oxide nanoparticles (IONPs) (Oceannanotech, LLS, Springdale, AR) via cross-linking of caboxyl groups of the amphilphilic polymer to the animo side groups of the peptides (Figure 1b) using our established protocol. Briefly, cysteine residues of ATF or BSA was subjected to reduction by TCEP (5 mM at pH 7.4 for 30 min at RT). Immediately after reduction, NIR830-maleimide dyes were added and allowed for conjugation for 4 hours at room temperature. The amphiphilic polymer-coated iron oxide nanoparticles (IONPs) were activated with ethyl-3-dimethyl amino propyl carbodiimide (EDAC) and sulfo-N-hydroxysuccinimide (sulfoNHS). The carboxyl group on the surface of activated IONP was then conjugated to the NIR-830-ATF or NIR-830-BSA ligands. Unconjugated peptides were removed by washing with 100 k spin columns for three times [24].

2.3 Animal tumor model

Mouse mammary tumor 4T1 cells (2×10^6) were implanted into mammary fat pads of 6–8 week-old BALB/C mice. Tumors were allowed to grow for 6–10 days to a size of 0.5–0.8 cm. Animals were anesthetized with a mixture of Ketamine (85 mg/kg) and Xylazine, and were sacrificed using University of Florida Institutional Animal Care and Use Committee (IACUC)-approved techniques. Strict animal care procedures approved by the University of Florida IACUC and based on guidelines from the NIH, guide for the Care and Use of Laboratory Animals were followed.

To investigate the feasibility of photoacoustic contrast enhancement with targeted NIR830-ATF-IONP, we performed in vivo PA imaging of 4T1 mouse mammary tumors using the following three groups of mice: 1) Group one ($n = 3$) received an uPAR targeted IONP targeting agent (100 pmol NIR830-ATF-IONP, 2) Group two ($n = 2$) received a non-targeted IONP agent conjugated with bovine serum albumin (BSA) (100 pmol NIR830-BSA-IONP), and 3) Group three ($n = 2$) received no IONP injection as control. Nanoparticle probes were injected via the tail vein.

2.4 Photoacoustic microscopy imaging system

The schematic of photoacoustic microscopy system was shown in Figure 2a. Two pulsed lasers were used in this study: 1) a tunable Ti : Sapphire laser (LT-2211A, LOTIS TII) with 8–30 nanosecond (ns) pulse duration and 10 Hz repetition rate for macroscopic imaging of tumors; and 2) a Nd : YAG laser

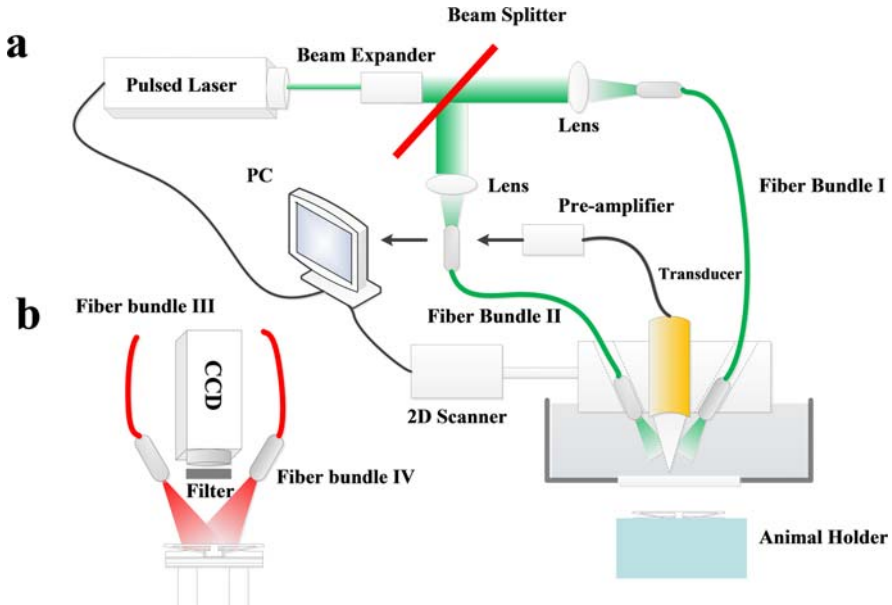

Figure 2 Schematic of imaging systems. (**a**) Schematic of photoacoustic microscopy imaging system. (**b**) Schematic of NIR fluorescence imaging system.

(NL 303HT from EKSPLA, Lithuania) with 6 ns pulse duration and 10 Hz repetition rate for microscopic imaging of the blood vessels. The laser beam was split and coupled into two optical fiber bundles separately which were both mounted and adjusted to allow optimal illumination in the imaging area. Induced photoacoustic waves were collected by a focused ultrasound transducer (50 MHz or 3.5 MHz). The 50 MHz transducer with 3 mm aperture and 6 mm focal length yields 30 μm resolution in axial and 60 μm resolution in lateral at the focal point. The 3.5 MHz transducer (V383, Olympus) with 15 mm aperture and 35 mm focal length yields axial and lateral resolution of 400 μm and 820 μm. The imaging probe, transducer and optical fiber bundles were mounted on a two-dimensional (2D) moving stage. One-dimensional depth-resolved images (A-line) at each transducer location were acquired and additional scanning along a transverse direction produced the 2D images referred to as B-scans. Further raster scanning along the other transverse direction enabled the reconstruction of 3D images. All photoacoustic images were displayed in maximum amplitude projection (MAP) form. All in vivo experiments were performed with a light intensity of 8 mJ/cm^2, which is lower than the American National Standards Institute safety limit of 20 mJ/cm^2.

2.5 Near-infrared planar fluorescence imaging system

As shown in Figure 2b two laser beams from separate 785 nm CW lasers (M5-785-0080, Thorlabs) were coupled into optical fiber bundle III and optical fiber bundle IV which were both fixed and adjusted for homogeneous illumination. A high-performance fluorescent band-pass filter (NT86-381, Edmund Optics) was mounted onto the front of a fast charge-coupled device camera (CoolSNAP EZ, Photometrics) which was used to collect the fluorescence signal. All experiments were conducted using the same power illumination and camera exposure times.

2.6 Image processing

Photoacoustic tomograms were reconstructed by a program implemented in Matlab 7.0 and merged with Amira 5.3.3. The photoacoustic signals collected were processed by the Hilbert transform before reconstruction, and the photoacoustic signals from each mouse were normalized to the same scale (0 ~ 256). Fluorescent images were collected by RS Image (Roper Scientific, Inc) provided by the manufacturer and processed by Matlab 7.0 and fused through Amira 5.3.3.

2.7 Histologic analysis

Tumors collected from mice were preserved in 10% neutral buffered formalin for 10 hours at room temperature. Histological sections were stained with Prussian blue staining and analyzed using standard procedures to confirm the presence of iron oxide nanoparticles.

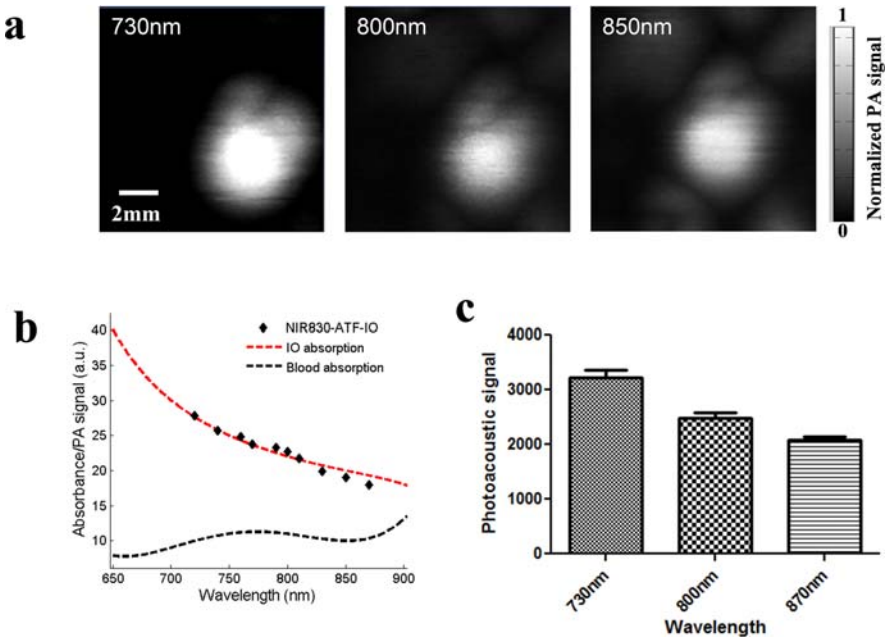

Figure 3 (**a**) *In vivo* MAP photoacoustic images of tumors using signals of 730 nm, 800 nm and 870 nm, 24 hours after injection of NIR830-ATF-IONP. (**b**) Absorption characteristics of NIR830-ATF-IONP, IONP and blood. (**c**) *In vivo* PA signals using different wavelength inputs.

2.8 Statistical analysis

All data obtained from the experiments were summarized using means ± standard error of the mean (SEM). All data points within a given field-of-view (FOV) (i.e., the tumor region in this study) were used to calculate the means/standard errors presented in this work. For the non-targeted or control tumors, four fiducial markers were used to indicate the FOV for the analysis.

3. Results

The absorbance of light by IONPs is much stronger compared to blood at wavelength longer than 650 nm. The absorbance of IONPs decreases with increasing wavelength (Figure 3b). Although the strongest absorption for IONPs lies near 650 nm, the appropriate wavelength for medical imaging is within the transparent optical window of 700–1000 nm, which increases the penetration depth. We measured the photoacoustic signal of NIR830-ATF-IONP at wavelengths from 730 nm to 870 nm (Figure 3b) and our findings agreed well with IONP absorption spectra presented by Galanzha [24]. Tumor-bearing mice were imaged at 24 hours after injection of NIR830-ATF-IONP and 730 nm was chosen as the best wavelength for in vivo photoacoustic imaging. From the MAP photoacoustic images shown in Figure 3a, NIR830-ATF-IONP-targeted tumors displayed the highest absorption at 730 nm compared to 800 nm and 850 nm. From the quantitative plot shown in

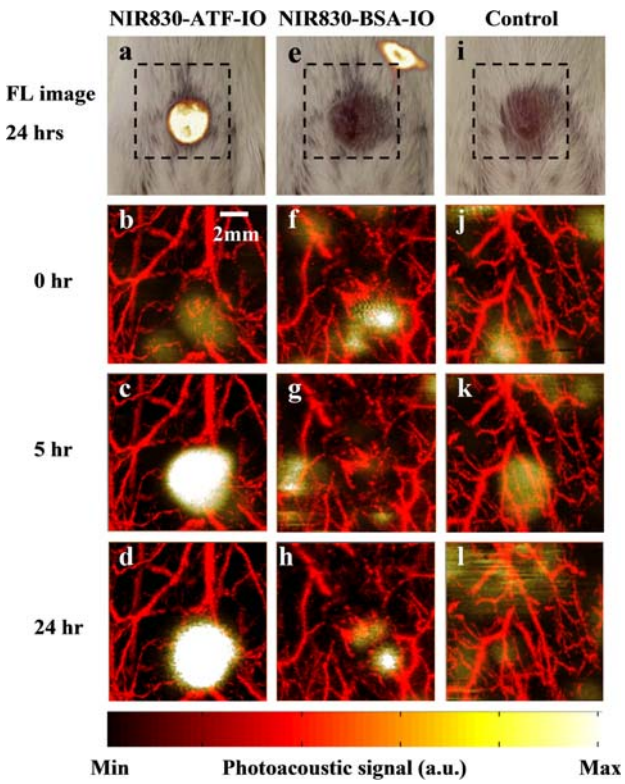

Figure 4 *In vivo* photoacoustic MAP and fluorescence images before and after injection. Micrographs were merged with fluorescence images taken 24 hours post injection with indicated agent (**a, e, i**). Panels **b** thru **l**. Photoacoustic MAP images were merged with images of blood vessels before injection (**b, f, j**), and at 5 hours (**c, g, k**) and 24 hours (**d, h, l**) hours post injection.

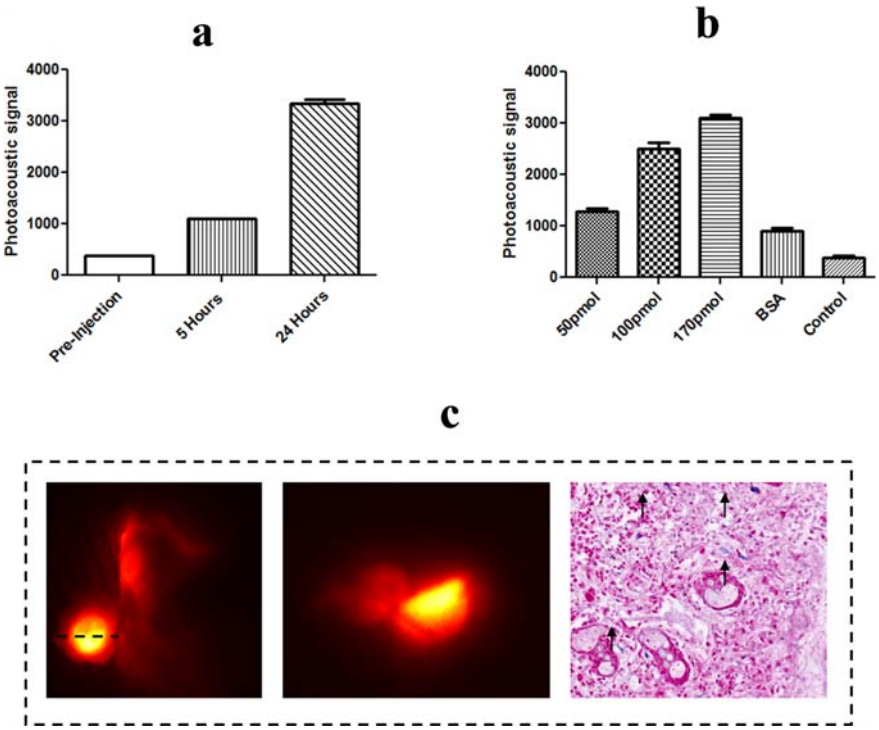

Figure 5 Quantitative plot and comparison of photoacoustic signals. (**a**) Photoacoustic signals before and after injection of NIR830-ATF-IONP. (**b**) Comparison of photoacoustic signals with different concentrations of injected NIR830-ATF-IONP. (**c**) NIR fluorescence imaging of resected tumor (**left** panel), cross-section of tumor along black dashed line (**middle** panel) and section stained with Prussian blue (**right** panel).

Figure 3c, the in vivo photoacoustic signal at 730 nm is 21% and 49% greater, compared to 800 nm and 870 nm, respectively. Similarly, the absorption of NIR830-ATF-IONP at 730 nm was 18% and 47% higher, compared to 800 nm and 870 nm, respectively. This *in vivo* data is consistent with *in vitro* signal enhancement studies.

As shown in Figure 4b, f, j, the contrast between tumor to normal tissue is low before injection. At 24 hours post NIR830-ATF-IONP injection the contrast increased significantly while there was no significant contrast increase using the non-targeted NIR830-BSA-IONP or in animals without injection (Figure 4 d, h, l). To verify the delivery of NIR830-ATF-IONP to tumor cells, NIR fluorescent images were collected before each photoaocustic experiment. We observed the strongest NIR signal in the tumor site at 24 hours post-injection for NIR830-ATF-IONP (Figure 4a) and the strongest NIR signal for NIR830-BSA-IONP was in the spleen (Figure 4e).

We plotted the photoacoustic enhancement in the tumor as a function of time in Figure 5a. The photoacoustic signals with NIR830-ATF-IONP increased 3 and 10 times at 5 and 24 hours post injection compared to non-injection control mice. This result indicates that NIR830-ATF-IONP accumulated in the tumors, as expected. Figure 5b shows the quantitative comparisons of photoacoustic signals in the tumor using different concentrations of NIR830-ATF-IONP. Compared with non-injection control mice, the photoacoustic contrast enhancement for 50 pmol, 100 pmol and 170 pmol is 300%, 1000% and 1200%, respectively (Figure 5b). The trend of photoacoustic signal enhancement over concentration was significantly different. Specifically, the photoacoustic signal increased steeply from 50 pM to 100 pM and then slowly from 100 pM to 170 pM. Tumors were resected and imaged by the NIR fluorescent system (Figure 5c). The NIR signal inside the tumor is strong and no NIR signals from the surrounding tissue or organs. The right panel of Figure 5c shows the histology section stained with Prussian blue staining. The arrow indicates the IONP cluster inside the tumor.

To evaluate the clinical utility of this technique, the imaging depth was investigated by adding biological tissues (chicken breast) to the top of the mice skin. Figure 6a (left) shows the MAP of the tumor in mice that received NIR830-ATF-IONP at 24 hours post-injection without adding chicken breast. The dashed red line represents the position of B-scan images shown in Figure 6c. Even after adding 31 mm of chicken breast (Figure 6a, right), the tumor is clearly seen in Figure 6c (d6). As the imaging depth increased, the signal to background ratio (SBR) decreased from 40 dB to 18 dB as shown in Figure 6b.

4. Discussion and summary

This work represents the first report on *in vivo* molecular photoacoustic tomography of breast cancer

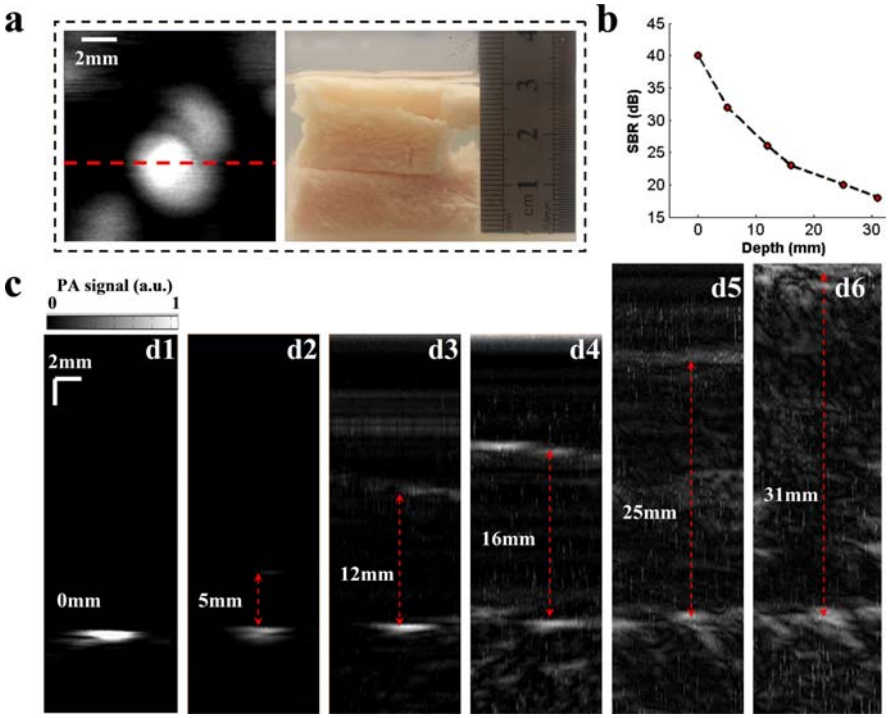

Figure 6 *In vivo* photoacoustic images with adding chicken breast between detector and tumor. (**a**) MAP image of tumor at 24 hours after injection without adding chicken breast (**left**) and photograph of 31 mm thick chicken breast (**right**). (**b**) SBR versus depth. (**c**) B-scan images by adding different thickness of chicken breast.

with receptor-targeted magnetic iron oxide nanoparticles in a mouse mammary tumor model. The photoacoustic signal enhancement for NIR830-ATF-IONP was 3 times higher compared to that for non-targeted NIR830-BSA-IONP and 10 times higher than the non-injection controls.

We compared IONP with other nanoparticles used as contrast agents for PAT in Table 1 [19–21, 24, 27–31]. From the detailed comparison, it is noted that IONP has modest absorption, smaller size (10 nm) and longer retention time, and can be used with small dose. These advantages make IONP a good contrast agent for photoacoustic imaging.

The uPAR-targeted IONP nanoparticle probe used in this study addresses some of the challenges for the use of targeted tumor imaging agents. Our methodology utilizes stable and high-affinity targeting ligands and produces strong imaging contrast for multi-image modalities. It has been shown that human breast cancer and tumor stromal cells have a higher level of uPAR receptor compared with other normal breast tissues [32, 33]. In addition, the highest level of uPAR receptor expression is detected in the invasive edge of the tumor region usually enriched in blood vessels making it accessible for uPAR receptor-targeted IONP in this area [34, 35]. The high-quality and uniformly sized IONPs used in this study were coated with a thin ampiphilic copolymer and have a relatively small particle complex (25 nm) which is more suitable for in vivo delivery of the imaging probe compared with other receptor-targeted or non-targeted nanoprobes for photoacoustic imaging [18, 19, 22]. It also has been shown that polymer-coated IONPs have more than 8 hours of plasma retention time [36] compared with other molecular imaging agents for PAT, which are usually less than 2 hours [18, 19, 22]. The delivery of NIR830-ATF-IONP to the

Table 1 Comparison of nanoparticles used as contrast agent for photoacoustic tomography.

Nanoparticles	Absorption*	Size	Retention time**	Dose	Multi mode
Iron oxide	Medium	10 nm (sphere)	>8 hours	pmol	PAT and MRI
Gold nanocage	Medium	50 nm	<5 hours	pmol–nmol	NA
Gold nanorod	High	52 nm × 15 nm	NA	nmol	NA
Gold nanoshell	High	140 nm	NA	pmol–nmol	NA
Gold nantotube	Medium	100 nm × 11 nm	NA	nmol	NA
Single-walled cabon nanotube	Low	186 nm × 1 nm	<2 hours	μmol	NA

* The wavelength range for the comparison is limited to between 680 nm and 800 nm.
** The retention time is estimated relative to the size of nanoparticles.

tumor was verified by planar NIR fluorescent imaging. This shows the potential for us to combine fluorescence molecular tomography (FMT) with photoacoustic tomography. While FMT has lower spatial resolution than PAT, it has higher specificity than photoacoustic imaging techniques and the combination of PAT and FMT would provide complementary information for breast cancer detection [26].

The demonstrated imaging depth of 31 mm indicates the potential of our method for tumor imaging in humans. While the photoacoustic system as described here is not yet suitable for clinical applications, it can be improved to be a clinical prototype using a commercial ultrasound array and/or a high frame rate of laser pulses with a high-speed scanning system [12].

By using high-frequency focused ultrasound transducer (>50 MHz), the microvasculature inside and around the tumor can be imaged as shown in Figure 4, indicating the potential of understanding the interplay between the tumor microvasculature and delivery of targeted contrast agents. We are also investigating multi-wavelength and quantitative PAT reconstruction methods to calculate functional parameters and nanoparticle concentrations in tissue. This will allow us to quantitatively study the delivery mechanism of NIR830-ATF-IONP through microvasculature to tumor tissue.

Acknowledgements We thank Dr. Andrew Y. Wang at Ocean Nanotech, LLC for providing magnetic iron oxide nanoparticles and Dr. Malgorzata Lipowska at Emory University for synthesis of NIR 830 dye. This research project was supported by the following NIH grants: NIH R21CA 161384 (Jiang) and R01CA133722 (Yang).

Conflicts of interest No potential conflicts of interest were disclosed.

Author biographies Please see Supporting Information online.

References

[1] A. Jemal, R. Siegel, E. Ward, Y. Hao, J. Xu, T. Murray, and M. J. Thun, CA Cancer. J. Clin. **58**, 71–96 (2008).
[2] American Cancer Society, American Cancer Society, Atlanta (2010).
[3] American Cancer Society, American Cancer Society, Atlanta (2011).
[4] P. A. Carney, D. L. Miglioretti, B. C. Yankaskas, K. Kerlikowske, R. Rosenberg, C. M. Rutter, B. M. Geller, L. A. Abraham, S. H. Taplin, M. Dignan, G. Cutter, and R. Ballard-Barbash, Ann. Intern. Med. **138**, 168–175 (2003).
[5] J. Smith and E. Andreopoulou, Ann. Oncol. **15**, i18–i26 (2004).
[6] D. Saslow, C. Boetes, W. Burke, S. Harms, M. O. Leach, C. D. Lehman, E. Morris, E. Pisano, M. Schnall, S. Sener, R. A. Smith, E. Warner, M. Yaffe, K. S. Andrews, and C. A. Russell, Cancer J. Clin. **57**, 75–89 (2007).
[7] T. F. Massoud and S. S. Gambhir, Genes. Dev. **17**, 545–580 (2003).
[8] M. Hofmann, Phys. Med. **21**, 11 (2006).
[9] F. Benard and E. Turcotte, Breast Cancer Res. **7**, 153–162 (2005).
[10] P. Beard, Interface Focus **1**, 602–631 (2011).
[11] S. Oladipupo, S. Hu, A. Santeford, J. Yao, J. R. Kovalski, R. V. Shohet, K. Maslov, L. V. Wang, and J. M. Arbeit, Blood **117**, 4142–4153 (2011).
[12] T. Erpelding, C. Kim, M. Pramanik, L. Jankovic, K. Maslov, Z. Guo, J. A. Margenthaler, M. D. Pashley, and L. V. Wang, Radiology **256**, 102–110 (2010).
[13] S. Manohar, A. Kharine, van J. C. G. Hespen, W. Steenbergen, and van T. G. Leeuwen, J. Biomed. Opt. **9**, 1172–1181 (2004).
[14] R. Kruger, R. Lam, D. Reinecke, S. Del Rio, and R. Doyle, Med. Phys. **37**, 6096–6100 (2011).
[15] L. Xi, J. Sun, Y. Zhu, L. Wu, H. Xie, and H. Jiang, Biomed. Opt. Express **1**, 1278–1283 (2010).
[16] L. Xi, S. Grobmyer, L. Wu, R. Chen, G. Zhou, L. G. Gutwein, J. Sun, W. Liao, Q. Zhou, H. Xie, and H. Jiang, Opt. Express **20**, 8726–8731 (2012).
[17] Y. Yuan, S. Yang, and D. Xing, Appl. Phys. Lett. **100**, 023702 (2011).
[18] C. Kim, K. H. Song, F. Gao, and L. V. Wang, Radiology **255**, 442–450 (2010).
[19] C. Kim, E. C. Cho, J. Chen, K. H. Song, L. Au, C. Favazza, Q. Zhang, C. M. Cobley, F. Gao, Y. Xia, and L. V. Wang, ACS nano **4**, 4559–4564 (2010).
[20] D. Pan, M. Pramanik, A. Senpan, J. S. Allen, S. A. Wickline, L. V. Wang, and G. M. Lanza, FASEB J. **25**, 875–882 (2011).
[21] X. M. Yang, S. E. Skrabalak, Z. Li, Y. Xia, and L. V. Wang, Nano Letters **7**, 3798–3802 (2007).
[22] A. D. L. Zerda, C. Zavaleta, S. Keren, S. Vaithilingam, S. Bodapati, Z. Liu, J. Levi, B. R. Smith, T. J. Ma, O. Oralkan, Z. Cheng, X. Chen, H. Dai, B. T. Khuri-Yakub, and S. S. Gambhir, Nat. Nanotech. **3**, 557–562 (2008).
[23] L. Yang, X. H. Peng, Y. A. Wang, X. Wang, Z. Cao, C. Ni, P. Karna, X. Zhang, W. C. Wood, X. Gao, S. Nie, and H. Mao, Clin. Cancer Res. **15**, 4722–4732 (2009).
[24] E. I. Galanzha, E. V. Shashkov, T. Kelly, J. W. Kim, L. Yang, and V. P. Zharov, Nat. Nanotech. **4**, 8558–8560 (2009).
[25] M. Lipowska, G. Patonay, and L. Strekowski, Synth. Commum. **23**, 3087–3094 (1993).
[26] B. Wang, Q. Zhao, N. Barkey, D. Morse, and H. Jiang, Med. Phys. **39**, 2512–2517 (2012).
[27] S. Manohar, C. Ungureanu, and T. G. Van Leeuwen, Contrast Media Mol. Imaging **6**, 389–400 (2011).
[28] W. Li, P. K. Brown, L. V. Wang, and Y. Xia, Contrast Media Mol. Imaging **6**, 370–377 (2011).

[29] L. Xiang, D. Xing, H. Gu, D. Yang, L. Zeng, and S. Yang, International Symposium on Biophotonics, Nanophotonics and Metamaterials, 2006, pp. 76–79.
[30] J. Kim, E. I. Galanzha, E. Shashkov, H. M. Moon, and V. P. Zharov, Nat. Nanotech **4**, 688–694 (2009).
[31] P. K. Jain, K. S. Lee, I. H. EI-Sayed, and M. A. EI-Sayed, J. Phys. Chem. B **110**, 7238–7248 (2006).
[32] S. DelVecchio, M. P. Stoppelli, M. V. Carriero, R. Fonti, O. Massa, P. Y. Li, G. Botti, M. Cerra, G. D'Aiuto, G. Esposito, and M. Salvatore, Cancer Res. **53**, 3198–3206 (1993).
[33] Y. Li, N. Wood, D. Yellowlees, and P. K. Donnelly, Anticancer Res. **19**, 1223–1228 (1999).
[34] E. Dublin, A. Hanby, N. K. Patel, R. Liebman, and D. Barnes, Am. J. Pathol. **157**, 1219–1227 (2000).
[35] A. Hemsen, L. Riethdorf, N. Brunner, J. Berger, S. Ebel, C. Thomassen, F. Jänicke, and K. Pantel, Int. J. Cancer **107**, 903–909 (2003).
[36] A. Moore, E. Marecos, A. Bogdanov Jr., and R. Weissleder, Radiology **214**, 568–574 (2000).